ELSEVIER

Physica C 333 (2000) 93–103

PHYSICA C

www.elsevier.nl/locate/physc

Grain texture and bulk magnetic anisotropy correlation in polycrystalline $Bi_2Sr_2CaCu_2O_{8+\delta}$ thin rods

E. Martínez [a], L.A. Angurel [a,*], J.C. Díez [a], A. Larrea [a], M. Aguiló [b], R. Navarro [a]

[a] *Instituto de Ciencia de Materiales de Aragón, CSIC-Universidad de Zaragoza, Centro Politécnico Superior de Ingenieros, María de Luna 3, 50015 Zaragoza, Spain*

[b] *Laboratori de Fisica Aplicada i Cristallografía, Universitat Rovira i Virgili, Tarragona, Spain*

Received 1 July 1999; accepted 13 January 2000

Abstract

The texture of Bi–Sr–Ca–Cu–O (BSCCO)-2212 polycrystalline thin rods, fabricated with a laser induced floating zone melting technique has been quantified and correlated with their bulk magnetic anisotropy. Scanning Electron Microscopy (SEM) determinations and X-ray Pole figure measurements on longitudinal and transverse cross-sections have been used to derive the spatial distribution of the crystallographic axes of the grains. The magnetic anisotropy has been deduced from the angular field dependence of the irreversible dc magnetisation. The correlation between these properties has been analysed in samples with a very different microstructure associated to slow and fast growth rates. © 2000 Elsevier Science B.V. All rights reserved.

PACS: 74.72.Hs; 74.80.Bj; 74.25.Ha; 74.60.Jg
Keywords: BSCCO; Texture; Magnetic anisotropy

1. Introduction

Laser Floating Zone (LFZ) melting techniques have enabled a fast and controlled growth of textured superconducting Bi–Sr–Ca–Cu–O (BSCCO) materials [1]. In particular, polycrystalline thin rods of the Bi-2212 phase with high critical currents at 77 K have been produced [2]. At a great extent, the ratio between growth speed, R, and temperature gradient at the solidification interface, G, controls the final microstructure [3]. The high G values reached in this technique, which are almost fixed by the laser focusing and the precursor material thermal conductivity, enable a broad variation of the R/G ratios producing grain size changes within two orders of magnitude and very different textures [4,5]. The anisotropic growth habits of BSCCO and related non-superconducting phases, which dispose particular crystallographic planes perpendicular to the solid–liquid interface (i.e., parallel to the temperature gradient), yield to textured thin rods adequate to develop hybrid current leads [6].

For LFZ processed thin rods, the average growth and texturing direction will coincide with the rod

* Corresponding author. Tel.: +34-976-761958; fax: +34-976-761957.
E-mail address: angurel@posta.unizar.es (L.A. Angurel).

0921-4534/00/$ - see front matter © 2000 Elsevier Science B.V. All rights reserved.
PII: S0921-4534(00)00030-7

axis [2], but the flatness of the solidification interface would determine the lack of parallelism of neighbouring grains. Thus, the different laser penetration and the local heating and dissipation intensity will modify the texture. Generally, any curvature on the solidifying interface can produce systematic misalignments of neighbouring grains [4].

On Bi-2212 single crystals, the extreme differences in magnitude, temperature and field dependencies of the critical current densities along the *c*-axis ($J_{c,c}$) and the *a*–*b* plane ($J_{c,ab}$) is well known [7,8]. Due to this anisotropy, $\Gamma_{grain} \approx 3000$ [9], for temperatures below a 3D to 2D crossover line, only the field component parallel to the *c*-axis, $H_{\|c}$, contributes to the dissipation [10]. Moreover, the platelet shape of the single crystals also give magnetic moments perpendicular to the *a*–*b* plane.

Polycrystalline textured materials have shown differences from single crystal behaviour reflected in shape effects, lower bulk anisotropy, Γ_{bulk}, and higher pinning energies [11]. This is reflected in the magnetic and transport measurements on two-dimensional textured materials, as it is in the case of $YBa_2Cu_3O_{7-x}$ and BSCCO-2212 thin films [12–15] or 2223–Ag sheathed tapes [16,17]. In these materials, shape and texture effects yield to J_c values only dependent on the perpendicular magnetic field component, $H_{\|c}$. All these effects reflect the influence of the microstructure in the magnetic response of these materials and the required deep knowledge of the relation between both properties.

In a previous work, the modifications in the microstructure induced by the growth conditions have been reported and used to describe quantitatively the changes in transport properties [5]. However, this performance directly depends on the grain junction strength and the current trajectories due to its percolate character, and only indirectly on the grain size and texture. To correlate the microstructure of textured polycrystalline materials with their macroscopic performances it would be more adequate to analyse the magnetic properties, in particular the anisotropy observed in magnetisation measurements. That is the objective of this contribution.

With this aim, the first part of this work is devoted to the quantification of the texture from Scanning Electron Microscopy (SEM) images and X-ray Pole figures, analysing also the change in texture occurring during heat treatments. In the second part, the differences observed in the magnetisation measurements, in particular, the evolution of the low temperature magnetic hysteresis loops for different field orientations has been reported. Finally, the relation between the bulk magnetic anisotropy and the texture of the samples is discussed. This study has been performed on samples with a very different microstructure.

2. Experimental details

Thin cylindrical monoliths or rods of 4 to 5 cm length and 0.5 mm radius, *r*, were produced following a LFZ procedure described elsewhere [4,18]. During the rod growth, a counter-rotation of 24 rpm between seeds and precursors was used in all cases. The behaviour of the two studied samples corresponds to opposite limits in the observed phenomenology [5]. Sample A, grown at $R = 15$ mm/h, is well textured with an R value chosen inside the interval of 15–30 mm/h, for which maximum transport current density values are obtained, $J_{c,tran}(77\ K) > 5500\ A/cm^2$ [5]. Sample B, grown at $R = 70$ mm/h, has a worse microstructure, with smaller grains and a poorer texture. These differences induce a transport critical current density that is three times lower than in sample A [5]. For each sample, pieces of 5 mm in length were used for magnetic and microstructural characterisations.

As-grown rods do not show superconducting behaviour at 77 K and need an additional annealing at 845–855°C in air for more than 12 h to ensure the disappearance of most secondary phases and to develop the superconducting Bi-2212 phase as the most abundant phase.

A SEM JEOL 6400 provided with a Link Analytical EDX spectrometer has been used to study the distribution of superconducting and secondary phases as well as the texture of as-grown and annealed samples. Annealed samples were polished and chemically etched at 0°C with 1 part of 60% perchloric acid mixed with 99 parts of 2-butoxy-ethanol during 30 s [19].

The almost homogeneous phase of annealed samples introduces difficulties in the quantitative SEM

analysis of the texture by the lack of contrast in the micrographs. For this reason, complementary X-ray Pole figures analysis has been applied in the study of the annealed samples by means of a Siemens D-5000 X-ray diffractometer equipped with a texture goniometer. In this case, the texture has been quantified from the (00 10) Pole figure measurements of polished longitudinal cross sections.

Magnetic measurements were performed in a SQUID magnetometer (Quantum Design). The samples were initially characterised using magnetic ac susceptibility, $\chi_{ac}(T)$ measurements at 120 Hz and field amplitudes of 0.1 mT parallel and perpendicular to the rod axis. Both samples exhibit critical temperatures, defined by the onset of diamagnetism, higher than 92 K, which do not depend on the field orientation.

3. Microstructure and quantification of the texture

The microstructure of both samples can be observed in the SEM backscattered electron images of Fig. 1 on longitudinal polished cross-sections. For as-grown samples (Fig. 1a and b) the black regions correspond to the $(Sr_{1-x}Ca_x)CuO_2$ oxide, while grey phases correspond to a Bi–Sr–Cu oxide (light grey) and a Bi-Sr-Ca-Cu one (dark grey). The $(Sr_{1-x}Ca_x)CuO_2$ oxide, which is the primary solidification phase, has a very fast kinetics and grows almost parallel to the rod axis, independently of the growth speed. Nevertheless, there is a significant difference on the orientation of BSCCO grains in both samples. In sample A ($R = 15$ mm/h), BSCCO grains tend to follow the orientation of those sec-

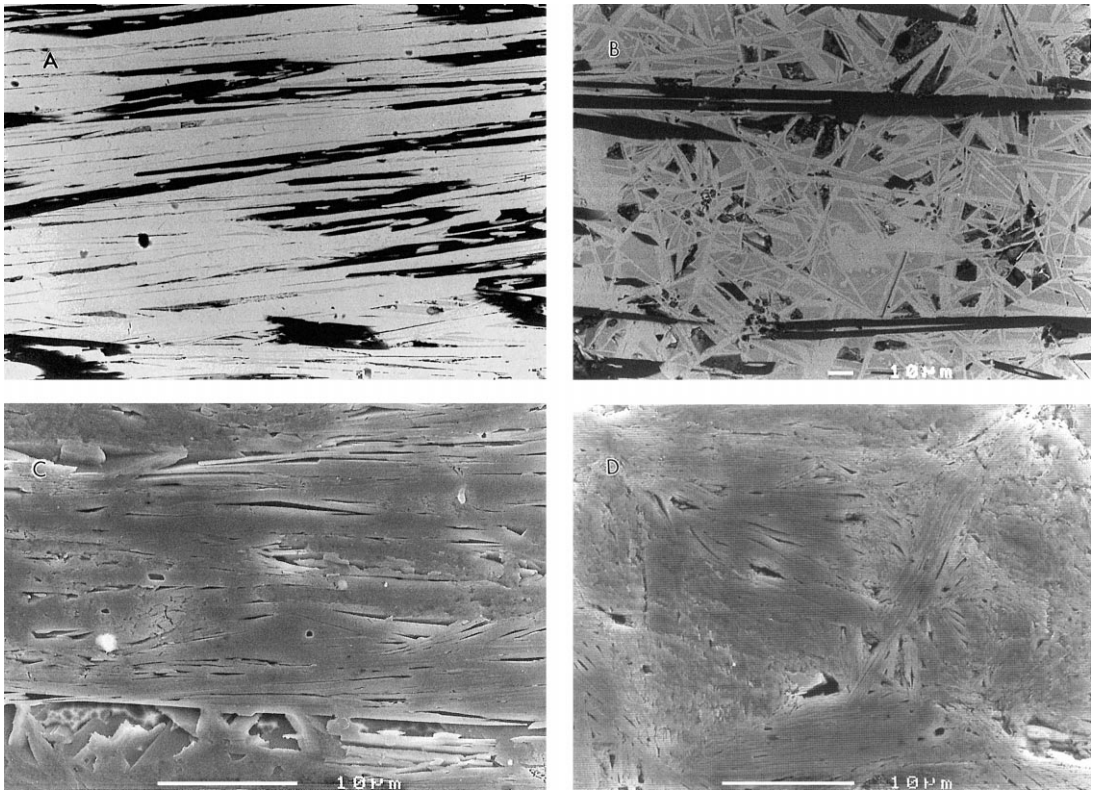

Fig. 1. SEM images of polished longitudinal cross sections of as-grown and annealed rods. For as grown rods of samples A (a) and B (b), backscattered electron images have been taken. For annealed samples A (c) and B (d), secondary electron images after chemical etching are displayed.

ondary phases (see Fig. 1a), whereas this is not the case in sample B, grown at 70 mm/h, where much higher disorder is present (see Fig. 1b).

In LFZ textured thin rods, the *c*-axis of the superconducting grains are disposed radially in a near random way [20], forming colonies whose *a–b* planes are mainly parallel. The mean dimensions of the colonies strongly depend on the growth speed. The length (parallel to the sample axis), width and thickness of these colonies in samples A and B are $100 \times 15 \times (1–8)$ and $20 \times 15 \times (1–3)$ μm^3, respectively. The thickness of isolated grains takes values of the order of 0.1–0.3 μm.

During the annealing the secondary phases are not longer chemically stable and the Bi-2212 phase becomes predominant by diffusion mechanisms [21], and the contrast of SEM images strongly decreases. As a consequence, to visualise the grains, the cross-sections have to be chemically etched (Fig. 1c and d).

3.1. Quantification of the texture from SEM micrographs

Through the analysis of digitised SEM micrographs of both transverse and longitudinal polished cross sections, it is possible to derive the spatial distribution of the *a–b* planes of the grains. This study gives a texture quantification and allows obtaining average estimations of the angle, θ, between the *a–b* planes and the external magnetic field applied to the sample.

This can be done for as-grown samples because of the good backscattered electron image contrast due to the presence of secondary phases. From the images of the longitudinal cross-sections it is possible to record the angles α_i formed by the $(Sr_{1-x}Ca_x)CuO_2$ grains and the rod axis (Fig. 2). These phases are elongated with their major geometrical axis almost parallel to the growth direction. In the transverse cross-section these grains have a polygonal shape [5]. It has been proposed that some epitaxial relationship can be found between the flat faces of these $(Sr_{1-x}Ca_x)CuO_2$ grains and the BSCCO grains [22]. Under this hypothesis of parallelism between secondary phases and BSCCO grains, these angles would correspond to the intersection lines between the *a–b* planes of the BSCCO grains

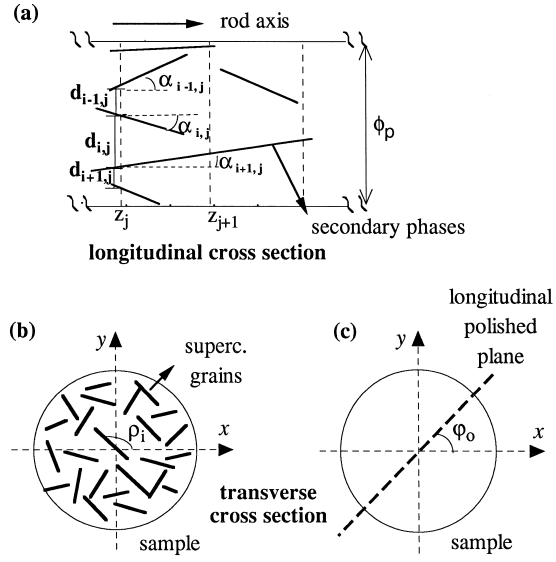

Fig. 2. Simplified scheme of the angles α_i, ρ_i and φ_0 derived from SEM images of longitudinal and transverse cross sections and used to calculate $\langle|\sin\theta|\rangle(\beta)$.

and the longitudinal polished plane. Note that this hypothesis is only valid in sample A, as it has previously been mentioned and therefore the following study has been performed only on this sample.

To derive the distribution of α_i through the sample, $P(\alpha)$, a process of four successive steps ($N_{SEM} = 4$) of parallel polishing and SEM observations were performed on the same 2 mm of length sample. For each longitudinal cross-section, the SEM images have been scanned and skeletonized by image processing to reduce the secondary phases to straight lines centred on the grains. In addition, a grid of equally spaced coordinates $z_j = j\Delta z$; $j = 1$ to N ($\Delta z = 10$ μm, $N = 200$) along the growth axis has been constructed (see Fig. 2a). On each cell of this grid, characterised by z_j, it is possible to derive an average angle by summation of finite elements extended to all intercepted lines,

$$\langle|\alpha|\rangle_p(z_j) = \frac{1}{\phi_p}\sum_{i=1}\frac{|\alpha_{i,j}| + |\alpha_{i+1,j}|}{2}d_{i,j}, \qquad (1.a)$$

where $d_{i,j}$, used as a relative weight, is the length of the segment intercepted in the z_j grid line by the adjacent i and $i+1$ secondary phase lines and verify that $\sum_i d_{i,j} = \phi_p$. Moreover, $\alpha_{i,j}$ is the angle be-

tween the i line of the cell j and the rod axis. Finally, the subindex p distinguishes the longitudinal sections of transverse length ϕ_p that have been analysed. The average misorientation angle of all grains of a given longitudinal section, $\langle|\alpha|\rangle_p$, is then calculated, adding up the results of all z_j values.

$$\langle|\alpha|\rangle_p = \frac{1}{N}\sum_{j=1}^{N}\langle|\alpha|\rangle_p(z_j). \qquad (1.b)$$

The following step is to average over all longitudinal N_{SEM} sections in order to obtain the average value over the whole sample, α_0:

$$\alpha_0 = \frac{\sum_{p=1}^{N_{SEM}}\langle|\alpha|\rangle_p\phi_p}{\sum_{p=1}^{N_{SEM}}\phi_p}. \qquad (2)$$

As expected for the observed conical distribution of the BSCCO grains, the value $\langle|\alpha|\rangle_p$ is almost independent of the section, with maximum differences of $\approx 1.5°$. In addition, the values of $\langle|\alpha|\rangle_p(z_j)$ through the cells of the grid only show minor random differences of 1–2°, confirming the homogeneity of the samples along the rod and confirming the consistency of this study because different pieces of the same rod have been used in microstructural and magnetic characterisations. From this analysis, it has been obtained that sample A exhibits a value of $\alpha_0 = 4.6°$ (with standard deviation of $\sigma_\alpha = 3°$).

On the other hand, from SEM images of a transverse cross section, the angle ρ_i, associated to the intersection lines of BSCCO grains with an arbitrary reference, may be determined (see Fig. 2b). In the following computations, this angle has been assumed to be continuously and uniformly distributed between 0 and π, as it is widely observed in these samples [5,18].

Any average of angular functions like $\sin\theta(\beta)$, β being the angle between the field and the rod's axis, can be obtained from the measured distribution of the angles α_i and ρ_i. This stereological problem has exactly been solved in three dimensions (see Appendix) improving previous 2D approximations developed for a similar texture study on superconducting tapes [17]. A particular interesting case correspond to $\beta = 0°$ ($\theta(\beta = 0) = \theta_0$), which gives the grain misorientation, and in consequence, the texture of the sample.

The distributions of α_i and ρ_i, experimentally obtained in two perpendicular cross-sections, are uncorrelated. Therefore, we have considered α and ρ as statistical independent variables. The angle φ_0 used to characterise the longitudinal polishing plane is assumed to be uniformly distributed in $[0, \pi]$.

Using Eq. (A.6) (see Appendix), the average $\langle|\sin\theta|\rangle$ is given by:

$$\langle|\sin\theta|\rangle = \int_{\rho=0}^{\pi}\int_{\varphi_0=0}^{\pi}\int_{\alpha=\alpha_{min}}^{\alpha=\alpha_{max}} \left|\frac{\sin\rho\sin\beta + \sin(\rho-\varphi_0)\cos\beta\tan\alpha}{\sqrt{1+\tan^2\alpha\sin^2(\rho-\varphi_0)}}\right| \frac{d\rho}{\pi}\frac{d\varphi_0}{\pi}P(\alpha)\,d\alpha. \qquad (3)$$

The results of $\langle|\sin\theta|\rangle(\beta)$ for different α_0 values and very narrow $P(\alpha)$ distributions ($\sigma_\alpha = 0$) are shown in Fig. 3. It is observed that the angular dependence of $\langle|\sin\theta|\rangle$ becomes stronger when α_0 decreases. Non-zero standard deviations, lower than α_0, produce small changes in the function $\langle|\sin\theta|\rangle(\beta)$, reducing the elbow observed at $\beta = \alpha_0$. These changes are more important when σ_α increases (see inset in Fig. 3). Moreover, for well

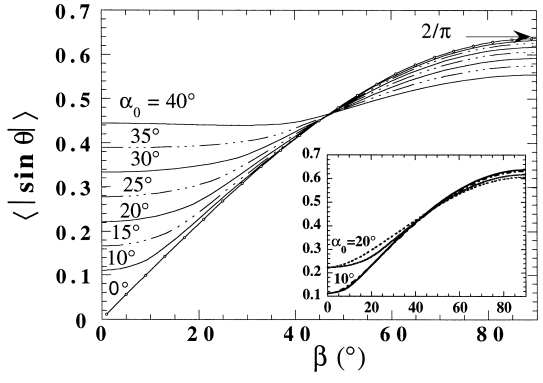

Fig. 3. Theoretical predictions of $\langle|\sin\theta|\rangle(\beta)$ for different average values of the misalignment angle $\langle|\alpha|\rangle = \alpha_0$ and $\sigma_\alpha = 0$. In the inset, the predictions of $\langle|\sin\theta|\rangle(\beta)$ for $\sigma_\alpha \neq 0$ (discontinuous line, $\alpha_0 = 10°$, $\sigma_\alpha = 5°$ and $\alpha_0 = 20°$, $\sigma_\alpha = 14°$) and for $\sigma_\alpha = 0$ (continuous line) are displayed.

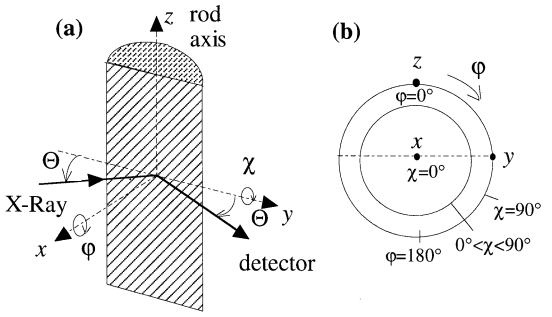

Fig. 4. (a) Geometrical arrangement of the X-ray Pole figures experiment on a longitudinal polished cross-section. (b) Angles χ and φ and the direction of the three main axes in a stereographic projection.

textured samples (i.e., low α_0 and small standard deviations) $\langle|\sin\theta|\rangle$ can be well approximated by $\approx(2/\pi)\sin\beta$ for $\beta>\alpha_0$ and $\approx(2/\pi)tg\,\alpha_0$ for $\beta<\alpha_0$. In particular, in sample A, in which $\alpha_0=$ 4.6°, $\langle|\sin\theta|\rangle(\beta=0°)=\langle|\sin\theta_0|\rangle=0.05$.

3.2. Quantification of the texture using X-ray Pole figures

To quantify the texture of the annealed samples, pole figures of the (00 10) reflection of the Bi-2212 phase on longitudinal polished cross sections have also been measured. The geometrical configuration of the measurements, the direction of the three main axes and the representation of the φ and χ angles in a stereographic projection are shown in Fig. 4a and b. The results of the X-ray Pole figures of both rods, after annealing, are displayed in Fig. 5a and b.

As expected from SEM results, sample A shows a narrower distribution of angles than sample B, which also displays a preferential orientation of *c*-axes. Note that for a fully textured sample, i.e., with the BSCCO *c*-axis at random but perpendicular to the sample axis, all intensity peaks would appear at $\varphi=\pm90°$ (discontinuous line in Fig. 4b). The observed reduction of the intensity values for χ higher than 50° in these experiments is due to the typical reduction of the measurement efficiency for high χ values [23].

To quantify the texture, it should be taken into account that the diffracted intensity at given angles, $I(\chi,\varphi)$, is proportional to the volume of crystallites in that direction [23]. The angle between the *a*–*b* planes and the rod axis, θ_0, can be written as a function of the spherical coordinates, χ and φ:

$$\sin\theta_0=\sin\chi\cos\varphi. \quad (4)$$

As $I(\chi,\varphi)$ is proportional to the probability density function to find grains with the *c*-axis pointing in the (χ,φ) orientation, the average values of any

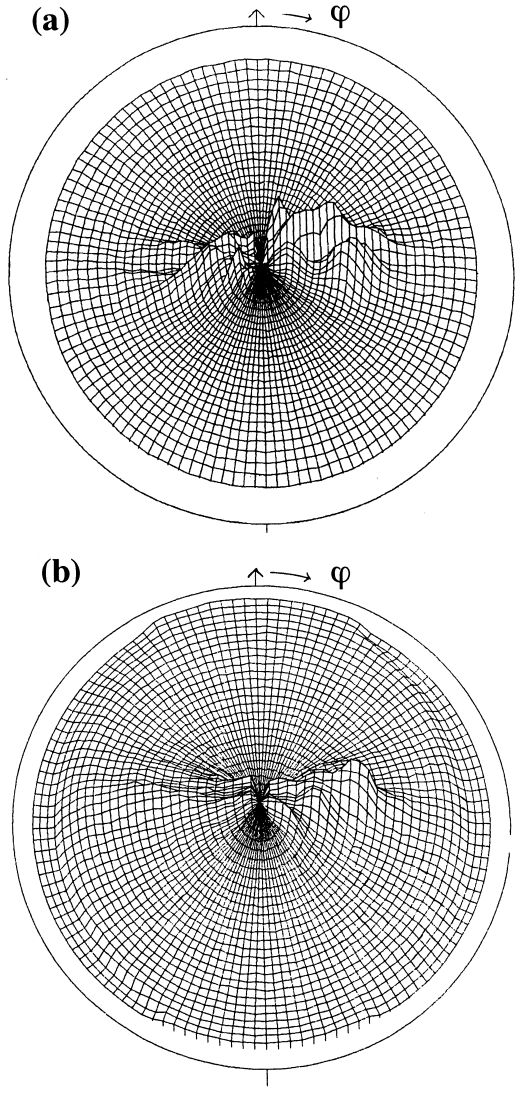

Fig. 5. X-ray Pole figures of the (00 10) reflection of a longitudinal cross-section in samples A (a) and B (b). Steps of 3° for the angles χ and φ was used.

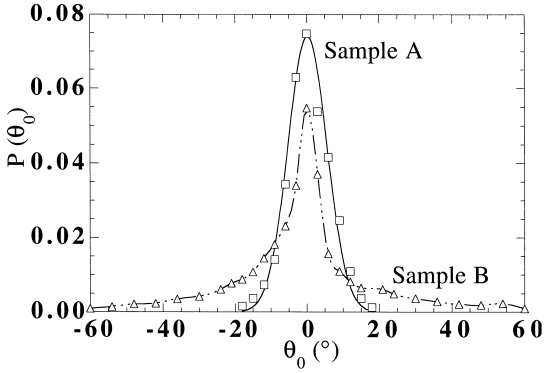

Fig. 6. Distribution of the angles $\theta(\beta = 0°) = \theta_0$, between the $a-b$ planes of the Bi-2212 superconducting grains and the rod axis of samples A (squares) and B (triangles) deduced from the Pole figures of the (00 10) reflection. The continuous line is a Gaussian distribution fit, while the discontinuous one is eye guide.

function of these angles can be obtained by simple averaging. There is always a background signal on $I(\chi,\varphi)$, which has been considered constant for values $\chi < 70°$ [23], and subtracted from the measured intensity. For this reason, just the data for $\chi < 70°$ have been considered in this estimation.

The probability density $P(\theta_0)$ to find superconducting grains forming angles with the rod axis between θ_0 and $\theta_0 + \mathrm{d}\theta_0$ is then given by:

$$P(\theta_0) = K\int_{\varphi=0}^{2\pi}\int_{\chi=0}^{2\pi}\delta\left[(\arcsin(\sin\chi\cos\varphi) - \theta_0\right] \times I(\chi,\varphi)\mathrm{d}\varphi\mathrm{d}\chi. \quad (5)$$

The values deduced from the Pole figures for both samples are plotted in Fig. 6. Now, the better texture of sample A is clearly observed as a narrower $P(\theta_0)$ function. In this sample the superconducting a–b planes are almost aligned with the rod axis with a Gaussian like distribution centred at $\langle\theta_0\rangle \approx 0°$ (cylindrical symmetry) and with $\sigma_0 \approx 5.5°$ (continuous line). In sample B, there are also grains aligned with the rod axis, but an important number with high θ_0 values ($> 10°$) still remains. In this sample, the distribution is also centred in $\langle\theta_0\rangle \approx 0°$, but with a standard deviation $\sigma_0 \approx 16°$, much higher than in the previous case. This result indicates the existence of texture in the annealed sample B, although poorer than in sample A (see Fig. 1c and d).

The estimated values of $\langle|\theta_0|\rangle$ and $\langle|\sin\theta_0|\rangle$ are:

Sample A $\langle|\theta_0|\rangle \approx 4.5°$, $\langle|\sin\theta_0|\rangle \approx 0.08$;

Sample B $\langle|\theta_0|\rangle \approx 13°$, $\langle|\sin\theta_0|\rangle \approx 0.20$.

From these results a value of $\alpha_0 \approx 8°$ for sample A, and of 20° for sample B are estimated. The former value is compatible with $\alpha_0 = 4.6°$ obtained in the above section from SEM analysis on as-grown sample A, but slightly higher. The lower values obtained from the SEM analysis may be associated to the considered approximation of full parallelism between non-superconducting and BSCCO grains, because there are regions where the full parallelism between secondary and superconducting phase grains is not maintained. In this case the α_0 value deduced from SEM would be underestimated. We may sug-

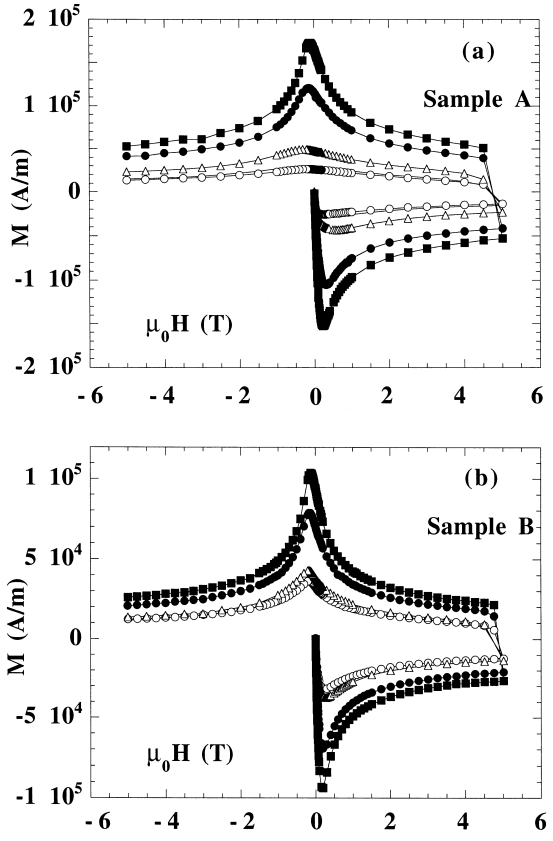

Fig. 7. Magnetic hysteresis loops of sample A (a) and B (b) at 5 K under different orientations of the external magnetic field: $\beta = 90°$ (full squares), 45° (full circles), 15° (open triangles) and 0° (open circles).

gest that during the annealing of well-textured samples, the grains' orientation remains mainly unchanged and appreciable texture improvements do not occur. The behaviour of sample B, which as grown is poorly textured, is different. X-ray Pole figure analysis indicates the development of texture in the Bi-2212 grains after annealing.

4. Magnetic anisotropy

To correlate the quantified microstructure and the bulk magnetic behaviour, magnetization measurements $M(H,\beta)$ at 5 K and for various field orientations have been performed. The results, displayed in Fig. 7, give a decrease of the magnetization with the external field orientation in both samples. Moreover, in agreement with the anisotropy results deduced from χ_{ac}, the angular dependence is bigger for the sample grown at the slowest growth speed. In case of sample A, $M(3\ \mathrm{T}, 0°)/M(3\ \mathrm{T}, 90°) = 4.2$, while a value of 2.5 has been obtained in case of sample B.

A rough estimation of the bulk anisotropy can be derived from the average values of the critical current density parallel and perpendicular to the rod axis. From the magnetization measurements at these orientations, Bean Critical State Model predictions

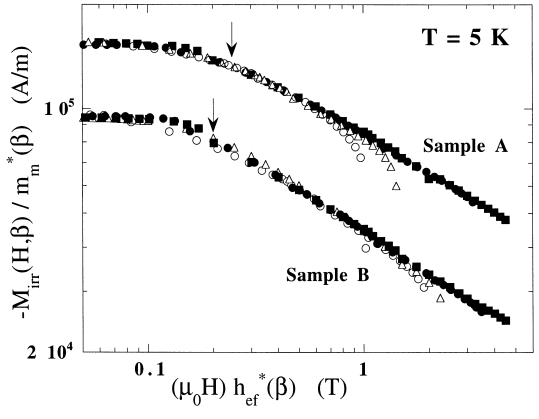

Fig. 8. Scaled values of the irreversible magnetisation at 5 K for both samples. The symbols have the same meaning as in Fig. 7. The arrows indicate the position of the magnetisation minimum at $\beta = 90°$.

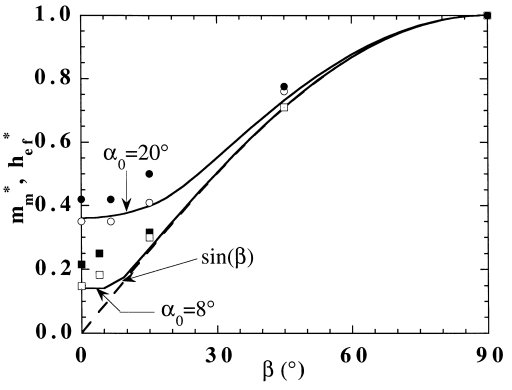

Fig. 9. Experimental scaling parameters $m_m^*(\beta)$ (open symbols) and $h_{ef}^*(\beta)$ (closed symbols) deduced from the $M_{irr}(H,\beta)$ measurements on sample A (squares) and B (circles). The continuous lines correspond to the theoretical predictions (see text) and the dashed one represents the $\sin(\beta)$ function.

give the relationships (see for instance Ref. [24] and references therein):

$$J_{c,\parallel} = (3/2)\Delta M_{\parallel}/r \quad \text{and} \quad J_{c,\perp} = (3\pi/8)\Delta M_{\perp}/r \tag{6}$$

where ΔM is the width of the hysteresis loop and r the sample radius. Therefore, it is possible to derive the bulk anisotropy values, $\Gamma_{bulk}(5\ \mathrm{K}) = 5.3$ (sample A), and 3.3 (sample B).

The study of the angular dependence of the irreversible magnetisation, M_{irr}, has been performed through the analysis of the M_{irr} scaling properties. As it is shown in Fig. 8, for each sample, all curves $M_{irr}(H,\beta)$ converge to only one when both axes (M_{irr} and H) are properly scaled. The magnetisation has been divided by an adimensional factor $m_m^*(\beta) = M_{irr}(0,\beta)/M_{irr}(0,90°)$, while the field has been multiplied by another adimensional factor, $h_{ef}^*(\beta)$, chosen in such a way that all curves coincide with the $\beta = 90°$ one in a wide range of fields. There are some discrepancies, mainly for sample A at small β and high fields, that correspond to situations at which the flux has not been totally reversed [18]. The scaling factors are shown in Fig. 9 for both rods. The observed scaling properties are common on anisotropic superconductors where the magnetic and electrical properties depend on an effective field, $H_{ef} \leq H$, which is related to the anisotropy [12–17]. The higher anisotropy of sample A in comparison to sample B, is clearly reflected by the stronger dependence of the scaling factors on β.

5. Discussion

The observed scaling in the magnetic properties can be related to the differences in texture of both samples. With this aim we consider a theoretical model in which the magnetic response of a superconducting Bi-2212 grain whose a–b planes form an angle θ_i with the external field would be analysed. Furthermore, magnetic fields high enough to fully penetrate all grains (i.e., $H > H_p$) would be studied because then the interaction between grains is expected to be small. In this limit the main contribution to the bulk magnetization of the rods should be granular and would be modelled as a distribution of independent grains.

For $0° < \beta < 90°$ the anisotropy yields to a magnetisation that is not parallel to the exciting field. In this case, the measured value $M_{\rm irr}$ is lower than $|M_{\rm irr}|$, because our SQUID magnetometer measures only the component parallel to H. In strongly anisotropic materials, $M_{\rm irr}$ has been found to be parallel to the c-axis except for $\theta_y \approx 0°$ [12,25]. Moreover, as several authors have pointed out, the existence of a component of $M_{\rm irr}$ perpendicular to H also depends on sample shape effects [26,27].

Under the hypothesis of non-interacting superconducting grains, the magnetisation of each grain, $M_{{\rm irr},i}$, would depend on the effective field acting on it, $H_{{\rm ef},i} \approx H\sin\theta_i$. On the other hand, the bulk magnetisation of the sample would be the average of the magnetisation of the grains parallel to the field:

$$M_{\rm irr} = \langle |\sin\theta| \cdot |M_{\rm irr}(H|\sin\theta|)| \rangle. \quad (7)$$

The derivation of the scaling factors $m^*_{\rm m}(\beta)$ and $h^*_{\rm ef}(\beta)$ from this equation requires some additional hypotheses on the field dependence of $M_{\rm irr}$. We have used the experimental potential behaviour observed at low temperatures, $M_{\rm irr} \propto H^{-q}$, where the exponent q takes the value $q = 0.4$ [18]. This allows the rewriting of Eq. (7) as

$$M_{\rm irr} = M_0(H\langle|\sin\theta|\rangle)^{-q}\langle|\sin\theta|^{1-q}\rangle\langle|\sin\theta|\rangle^q$$
$$= M_0(Hh_{\rm ef})^{-q} m_{\rm m} \quad (8)$$

which certainly gives the same field power law dependence and the expressions for the scaling factors: $h_{\rm ef}(\beta) = \langle|\sin\theta|\rangle$ and $m_{\rm m}(\beta) = \langle|\sin\theta|^{1-q}\rangle \times \langle|\sin\theta|\rangle^q$.

In order to compare the theoretical predictions of the scaling factors with the above experimental results, we have calculated the values of $h^*_{\rm ef}(\beta) = h_{\rm ef}(\beta)/h_{\rm ef}(90°)$ and $m^*_{\rm m}(\beta) = m_{\rm m}(\beta)/m_{\rm m}(90°)$ represented by continuous lines in Fig. 9. A potential field dependence with $q = 0.4$ and an angular distribution characterised by $\alpha_0 = 8°$ and $\alpha_0 = 20°$ as obtained in the Pole figure studies has been used. The similarity of these scaling factors with the function $\langle|\sin\theta|\rangle^*(\beta) = \langle|\sin\theta|\rangle(\beta)/\langle|\sin\theta|\rangle(90°)$ should be noted.

Considering the parameters that have been used, the practical coincidence of the $h^*_{\rm ef}(\beta)$ and $m^*_{\rm m}(\beta)$ theoretical predictions is noticeable. Moreover, it also should be remarked that the predictions for $\alpha_0 = 8°$ (well-textured samples) almost coincide with the function $\sin\beta$ (dashed lines in Fig. 9), in a wide range of angles. This means that in well-textured samples and for high β angles, the misorientation is so small that in average the response of the sample is determined by the angle that forms the external magnetic field and the sample axis. In the case of sample B, the bad texture determines the magnetic behaviour even for high β values.

On the experimental side, however, the values of $h^*_{\rm ef}(\beta)$ are always slightly higher than those of $m^*_{\rm m}(\beta)$, with increased differences at low β values. Furthermore, theoretical predictions of the scaling factors, derived with a very narrow distribution around the average values, reproduce approximately the observed behaviour, but also increase the discrepancies at low β values. This fact would indicate that it is necessary to introduce a more realistic angular distribution in the analysis, although the main conclusions will remain unaffected.

6. Conclusions

SEM and X-ray Pole figure measurements have been used to derive and quantify the distribution of angles $\theta_i(\beta)$ between the a–b planes of the Bi-2212 grains and the external magnetic field, which forms an angle β with the sample axis ($0 \le \beta \le 90°$) in polycrystalline LFZ textured thin rods. Macroscopic average values of $\langle|\theta|\rangle(\beta)$ and $\langle|\sin\theta|\rangle(\beta)$ have been derived, which for $\beta = 0°$ give the texture

quality of each sample. As it was expected, this quality improves when the growth rate decreases.

The analysis of SEM pictures in as-grown samples and of X-ray Pole figures in annealed rods, have been used to follow the evolution of the texture. On well-textured samples, the alignment of the BSCCO grains does not improve with annealing and only adjustments of the Bi-2212 phase stoichiometry, induced by diffusion, take place. However, on samples grown at high rates some texture is induced during the annealing and the Bi-2212 grains tend to be oriented in the direction of the non-superconducting phases observed in the as-grown samples.

A strong quantitative correlation between the bulk magnetic anisotropy and the grains a–b plane misalignment with respect to the rod axis has been found. The angular dependence of the irreversible magnetisation is enhanced for low growth speed. Moreover, all $M_{\rm irr}(H,\beta)$ curves stack upon the same curve, using scaling factors, $m^*_{\rm m}(\beta)$ and $h^*_{\rm ef}(\beta)$, which have been quantitatively correlated with the measured misorientation average angles. In consequence, the origin of the anisotropy in the magnetic properties is the texture of the sample, existing a clear correspondence between the grains misalignment to respect to the rod axis and the magnetic anisotropy observed in these samples.

Acknowledgements

The authors are indebted to the Spanish Ministerio de Educación y Ciencia (CICYT, MAT 95-0921-C02-01 and 02), the CICYT and the European Community (Project 2FD97-0546-C04-01) the MIDAS program and RED ELECTRICA DE ESPAÑA (Project REE-ID-97017) for financial support of this research. E. Martínez thanks the Spanish Ministerio de Educación y Ciencia for a scholarship.

Appendix A. Derivation of the macroscopic average $\langle|\sin\theta|\rangle(\beta)$ from grain orientation measurements in SEM observations

To calculate the distribution of angles, θ_i, formed by an external magnetic field and the a–b planes of the BSCCO grains, the input needed are the angle between the external magnetic field and the rod axis, β, and the misorientation angles measured on SEM longitudinal (α_i) and transverse (ρ_i) polished cross-section micrographs (see Fig. 2).

As BSCCO grains are platelets perpendicular to the c-axis, a simple characterisation of the orientation can be performed using unitary vectors, $\boldsymbol{n}_i$, parallel to the c-axis of components $(n_{xi},\ n_{yi},\ n_{zi})$. In addition, a convenient reference is to choose as the z-axis the rotational symmetry and the field $\boldsymbol{H}$ contained in the x–z plane; i.e., of components $(H\sin\beta,\ 0,\ H\cos\beta)$. Then, the angle θ_i may be derived from the scalar product of $\boldsymbol{n}_i\cdot\boldsymbol{H}$ by:

$$\sin\theta_i=\frac{\boldsymbol{n}_i\cdot\boldsymbol{H}}{H}=n_{xi}\sin\beta+n_{zi}\cos\beta \qquad (A.1)$$

where the n_{xi} and n_{zi} components should be written as a function of the misorientation angles α_i and ρ_i derived from SEM observations.

Longitudinal planes, which are parallel to the rod axis, can be characterised by a unitary vector $\boldsymbol{n}_0$ of components $(\sin\varphi_0,\ \cos\varphi_0,\ 0)$. Due to the cylindrical symmetry, φ_0 is a random variable uniformly distributed in the interval $[0,\pi]$. The straight lines observed in SEM longitudinal cross-sections correspond to the intersection of the polishing plane and the a–b plane of superconducting grains and are parallel to the product $\boldsymbol{n}_0\times\boldsymbol{n}_i$. Accordingly, the angle α_i measured in the micrographs is related to the projection of this product along the z-axis (characterised by the $\boldsymbol{u}_z$ unitary vector):

$$\cos\alpha_i=\frac{(\boldsymbol{n}_0\times\boldsymbol{n}_i)\cdot\boldsymbol{u}_z}{|\boldsymbol{n}_0\times\boldsymbol{n}_i|}=\frac{n_{xi}\cos\varphi_0+n_{yi}\sin\varphi_0}{\sqrt{n_{zi}^2\cos^2\varphi_0+n_{zi}^2\sin^2\varphi_0+(n_{xi}\cos\varphi_0+n_{yi}\sin\varphi_0)^2}} \qquad (A.2)$$

which is equivalent to:

$$n_{zi}=\pm\left(n_{xi}\cos\varphi_0+n_{yi}\sin\varphi_0\right)\tan\alpha_i. \qquad (A.3)$$

On the other hand, in SEM transverse cross-sections, the intersection of the polishing plane and the a–b plane of grains defines straight lines pointing in the $\boldsymbol{u}_z\times\boldsymbol{n}_i$ directions. The angle ρ_i between these lines and the x-axis (see Fig. 2b) relates n_{xi} to n_{yi} by:

$$n_{xi}=-n_{yi}\tan\rho_i. \qquad (A.4)$$

Combining these results, Eq. (A.1) may be finally rewritten as a function of the φ_0, ρ_i and α_i angles:

$$\sin\theta_i = \frac{\boldsymbol{n}_i \cdot \boldsymbol{H}}{H} = n_{xi}\sin\beta + n_{xi}\cos\beta \qquad (A.5)$$

and, in consequence, the average $\langle|\sin\ \theta|\rangle(\beta)$ is given by

$$\langle|\sin\theta|\rangle = \int_{\rho=0}^{\pi}\int_{\varphi_0=0}^{\pi}\int_{\alpha=\alpha_{\min}}^{\alpha=\alpha_{\max}} \left|\frac{\sin\rho\sin\beta + \sin(\rho-\varphi_0)\cos\beta\tan\alpha}{\sqrt{1+\tan^2\alpha\sin^2(\rho-\varphi_0)}}\right| \frac{\mathrm{d}\rho}{\pi}\frac{\mathrm{d}\varphi_0}{\pi}P(\alpha)\mathrm{d}\alpha. \qquad (A.6)$$

References

[1] R.S. Feigelson, D. Gazit, D.K. Fork, T.H. Geballe, Science 240 (1988) 1642.
[2] L.A. Angurel, G.F. de la Fuente, A. Badía, A. Larrea, J.C. Díez, J.I. Peña, E. Martínez, R. Navarro, in: A. Narlikar (Ed.), Studies of High Temperature Superconductors Vol. 21 Nova Science Publishers, 1997, p. 1.
[3] W. Kurz, D.J. Fisher, Fundamentals of Solidification, Trans. Tech. Publication, Switzerland, 1992.
[4] G.F. de la Fuente, J.C. Díez, L.A. Angurel, J.I. Peña, A. Sotelo, R. Navarro, Adv. Mater. 7 (1995) 853.
[5] L.A. Angurel, J.C. Díez, E. Martínez, J.I. Peña, G.F. de la Fuente, R. Navarro, Physica C 302 (1998) 39.
[6] L.A. Angurel, J.C. Diez, H. Miao, E. Martínez, G.F. de la Fuente, R. Navarro, Inst. Phys. Conf. Ser. No. 158 (1997) 1211.
[7] P. Schmitt, L. Schultz, G. Saemann-Ischenko, Physica C 168 (1990) 475.
[8] S. Luo, G. Yang, C.E. Gough, Phys. Rev. B 51 (1995) 6655.
[9] D.E. Farrell, S. Bonham, J. Foster, Y.C. Chang, P.Z. Jiang, K.G. Vandervoort, D.J. Lam, V.G. Kogan, Phys. Rev. Lett. 63 (1989) 782.
[10] P.H. Kes, J. Aarts, V.M. Vinokur, C.J. van der Beek, Phys. Rev. Lett. 64 (1990) 1063.
[11] E. Martínez, L.A. Angurel, J.C. Díez, F. Lera, R. Navarro, Physica C 271 (1996) 133.
[12] H. Teshima, A. Oishi, H. Izumi, K. Ohata, T. Morishita, S. Tanaka, Appl. Phys. Lett. 58 (1991) 2833.
[13] P. Schmitt, P. Kummeth, L. Schultz, G. Saemann-Ischendo, Phys. Rev. Lett. 67 (1991) 267.
[14] A. Geerkens, M. Meven, H.J. Frenck, Physica C 235–240 (1994) 3067.
[15] H. Raffy, S. Labdi, O. Laborde, P. Monceau, Phys. Rev. Lett. 66 (1991) 2515.
[16] B. Hensel, J.C. Grivel, A. Jeremie, A. Perin, A. Pollini, R. Flükiger, Physica C 205 (1993) 329.
[17] Q.H. Hu, H.W. Weber, H.K. Liu, S.X. Dou, H.W. Neumüller, Physica C 252 (1995) 211.
[18] E. Martínez, L.A. Angurel, J.C. Díez, R. Navarro, Physica C 289 (1997) 1.
[19] Y. Feng, K.E. Hautanen, Y.E. High, D.C. Larbalestier, R. Ray II, E.E. Hellstrom, S.E. Babcock, Physica C 192 (1992) 292.
[20] E. Snoeck, A. Larrea, C. Roucau, G.F. de la Fuente, Y. Huang, Physica C 198 (1992) 129.
[21] A. Larrea, E. Snoeck, A. Badía, G.F. de la Fuente, R. Navarro, Physica C 220 (1994) 21.
[22] F.M. Costa, R.F. Silva, J.M. Vieira, Physica C 289 (1997) 161.
[23] H.R. Wenk, in: Preferred Orientation in Deformed Metals and Rocks: An Introduction to Modern Texture Analysis, Academic Press, University of California, Berkeley, CA, 1985, pp. 33–37.
[24] R.B. Goldfarb, M. Lelental, C.A. Thomson, in: R.A. Hein (Ed.), Magnetic Susceptibility of Superconductors and Other Spin Systems, Plenum, New York, 1991, pp. 49–80.
[25] L. Fruchter, C. Aguillon, S. Senoussi, I.A. Campbell, Physica C 160 (1989) 185.
[26] F. Hellman, E.M. Gyorgy, R.C. Dynes, Phys. Rev. Lett. 68 (1992) 867.
[27] H. Theuss, T. Becker, H. Kronmüller, Physica C 233 (1994) 179.